TESS Spots a Hot Jupiter with an Inner Transiting Neptune

N.B. When citing this work, cite the original published paper.

(article starts on next page)

CrossMark

TESS Spots a Hot Jupiter with an Inner Transiting Neptune

Chelsea X. Huang[1,33], Samuel N. Quinn[2], Andrew Vanderburg[3,34], Juliette Becker[4,35], Joseph E. Rodriguez[2], Francisco J. Pozuelos[5,6], Davide Gandolfi[7], George Zhou[2,36], Andrew W. Mann[8], Karen A. Collins[2], Ian Crossfield[1,9], Khalid Barkaoui[6,10], Kevin I. Collins[11], Malcolm Fridlund[12,21], Michaël Gillon[6], Erica J. Gonzales[13,37], Maximilian N. Günther[1,33], Todd J. Henry[22], Steve B. Howell[23], Hodari-Sadiki James[25], Wei-Chun Jao[25], Emmanuël Jehin[5], Eric L. N. Jensen[26], Stephen R. Kane[27], Jack J. Lissauer[23], Elisabeth Matthews[1], Rachel A. Matson[15], Leonardo A. Paredes[25], Joshua E. Schlieder[17], Keivan G. Stassun[28,29], Avi Shporer[1], Lizhou Sha[1], Thiam-Guan Tan[30], Iskra Georgieva[12], Savita Mathur[20], Enric Palle[31], Carina M. Persson[12], Vincent Van Eylen[32], George R. Ricker[1], Roland K. Vanderspek[1], David W. Latham[2], Joshua N. Winn[24], S. Seager[1,16,14], Jon M. Jenkins[18], Christopher J. Burke[19], Robert F. Goeke[1], Stephen Rinehart[17], Mark E. Rose[18], Eric B. Ting[18], Guillermo Torres[2], and Ian Wong[16,35]

[1] Department of Physics, and Kavli Institute for Astrophysics and Space Research, Massachusetts Institute of Technology, Cambridge, MA 02139, USA
[2] Center for Astrophysics, Harvard & Smithsonian, 60 Garden Street, Cambridge, MA 02138, USA
[3] Department of Astronomy, The University of Texas at Austin, Austin, TX 78712, USA
[4] Division of Geological and Planetary Sciences, California Institute of Technology, Pasadena, CA 91125, USA
[5] Space Sciences, Technologies and Astrophysics Research (STAR) Institute, Université de Liège, 19C Allée du 6 Août, B-4000 Liège, Belgium
[6] Astrobiology Research Unit, Université de Liège, 19C Allée du 6 Août, B-4000 Liège, Belgium
[7] Dipartimento di Fisica, Università degli Studi di Torino, via Pietro Giuria 1, I-10125, Torino, Italy
[8] Department of Physics and Astronomy, University of North Carolina at Chapel Hill, Chapel Hill, NC 27599, USA
[9] Department of Physics and Astronomy, University of Kansas, 1251 Wescoe Hall Drive, Lawrence, KS 66045, USA
[10] Oukaimeden Observatory, High Energy Physics and Astrophysics Laboratory, Cadi Ayyad University, Marrakech, Morocco
[11] George Mason University, 4400 University Drive, Fairfax, VA 22030, USA
[12] Department of Space, Earth and Environment, Chalmers University of Technology, Onsala Space Observatory, SE-439 92 Onsala, Sweden
[13] Department of Astronomy and Astrophysics, University of California, Santa Cruz, 1156 High Street, Santa Cruz, CA 95064, USA
[14] Department of Aeronautics and Astronautics, MIT, 77 Massachusetts Avenue, Cambridge, MA 02139, USA
[15] U.S. Naval Observatory, Washington, DC 20392, USA
[16] Department of Earth, Atmospheric and Planetary Sciences, Massachusetts Institute of Technology, Cambridge, MA 02139, USA
[17] NASA Goddard Space Flight Center, Greenbelt, 8800 Greenbelt Road, MD 20771, USA
[18] NASA Ames Research Center, Moffett Field, CA 94035, USA
[19] Kavli Institute for Astrophysics and Space Research, Massachusetts Institute of Technology, Cambridge, MA, USA
[20] Instituto de Astrofisica de Canarias, c/Via Lactea s/n, E-38205 La Laguna Santa Cruz de Tenerife, Spain
[21] Leiden Observatory, University of Leiden, Leiden, The Netherlands
[22] RECONS Institute, Chambersburg, PA 17201, USA
[23] Space Science & Astrobiology Division, NASA Ames Research Center, Moffett Field, CA 94035, USA
[24] Department of Astrophysical Sciences, Princeton University, 4 Ivy Lane, Princeton, NJ 08544, USA
[25] Georgia State University, Atlanta, GA 30302, USA
[26] Dept. of Physics & Astronomy, Swarthmore College, Swarthmore, PA 19081, USA
[27] Department of Earth and Planetary Sciences, University of California, Riverside, CA 92521, USA
[28] Vanderbilt University, Department of Physics & Astronomy, 6301 Stevenson Center Lane, Nashville, TN 37235, USA
[29] Fisk University, Department of Physics, 1000 18th Avenue North, Nashville, TN 37208, USA
[30] Perth Exoplanet Survey Telescope, Perth, Western Australia, Australia
[31] Instituto de Astrofisica de Canarias, Via Lactea sn, E-38200, La Laguna, Tenerife, Spain
[32] Mullard Space Science Laboratory, Department of Space and Climate Physics, University College London, UK

Abstract

Hot Jupiters are rarely accompanied by other planets within a factor of a few in orbital distance. Previously, only two such systems have been found. Here, we report the discovery of a third system using data from the *Transiting Exoplanet Survey Satellite* (*TESS*). The host star, TOI-1130, is an eleventh magnitude K-dwarf in *Gaia G*-band. It has two transiting planets: a Neptune-sized planet ($3.65 \pm 0.10\,R_\oplus$) with a 4.1 days period, and a hot Jupiter ($1.50^{+0.27}_{-0.22}\,R_J$) with an 8.4 days period. Precise radial-velocity observations show that the mass of the hot Jupiter is $0.974^{+0.043}_{-0.044}\,M_J$. For the inner Neptune, the data provide only an upper limit on the mass of $0.17\,M_J$ (3σ). Nevertheless, we are confident that the inner planet is real, based on follow-up ground-based photometry and adaptive-optics imaging that rule out other plausible sources of the *TESS* transit signal. The unusual planetary architecture of and the brightness of the host star make TOI-1130 a good test case for planet formation theories, and an attractive target for future spectroscopic observations.

Unified Astronomy Thesaurus concepts: Exoplanet astronomy (486); Extrasolar gas giants (509); Extrasolar rocky planets (511); Exoplanets (498); Hot Jupiters (753)

[33] Juan Carlos Torres Fellow.
[34] NASA Sagan Fellow.
[35] 51 Pegasi b Fellow.
[36] NASA Hubble Fellow.
[37] NSF Graduate Research Fellow.

1. Introduction

The origin of gas giants on extremely short-period orbits has been an unsolved problem for 25 yr (Mayor & Queloz 1995). Although many scenarios have been proposed to place these hot

Jupiters in their current orbital locations (disk migration, in situ formation, planet–planet scattering, secular migration, etc.), no single mechanism seems capable of satisfying all the observational constraints (Dawson & Johnson 2018). One clue is that hot Jupiters tend to be "lonely," in the sense that stars with hot Jupiters often have wide-orbiting companions (Schlaufman & Winn 2016) but tend to lack nearby planetary companions within a factor of 2 or 3 in orbital distance (Steffen et al. 2012). The only known exceptions are WASP-47 and Kepler-730 (Becker et al. 2015; Zhu et al. 2018; Cañas et al. 2019).

How should these two systems be understood? Are they simply rare variants of hot Jupiters? Or did they form by a different process—perhaps the same process that led to the formation of "warm Jupiters" ($P = 20$–100 days), which are often flanked by smaller companions (Huang et al. 2016)? The *Transiting Exoplanet Survey Satellite* (*TESS*; Ricker et al. 2015) is well suited to address these questions by discovering more systems like WASP-47 and Kepler-730. By observing most of the sky, *TESS* is expected to find thousands of hot Jupiters (Sullivan et al. 2015), while also having good enough photometric precision to find smaller planets around the same stars (see, e.g., Huang et al. 2018), especially those with short orbital periods.

Here, we report the discovery of one such system: TOI-1130. It is only the third star known to have a transiting giant planet with an orbital period shorter than 10 days as well as a second transiting planet. The host star is brighter than the host stars of the previously known systems, especially at infrared wavelengths, which should provide good opportunities to study this type of system in detail. The newly discovered hot Jupiter also has a somewhat longer period (8.4 days) than WASP-47 (4.2 days) and Kepler-730 (6.5 days). Thus, TOI-1130 may serve as a bridge connecting WASP-47 and Kepler-730 to longer-period giant planets.

Section 2 of this Letter presents the *TESS* photometric data, as well as the follow-up observations that validated both planet detections and led to the measurement of the mass of the hot Jupiter. Section 3 describes our methods for determining the system parameters. Section 4 discusses the dynamical interactions between the two planets, as well as the possible implications this system will have on our understanding of hot Jupiter formation.

2. Observations and Data Reduction

2.1. TESS *Photometry*

TOI-1130 (TIC 254113311; Stassun et al. 2019) was observed by *TESS* on charge-coupled device (CCD) 2 of Camera 1 between 2019 June 19 and July 18, in the thirteenth and final sector of the survey of the southern ecliptic hemisphere. The star had not been pre-selected for 2 minute time sampling, and hence the only available data are from the full-frame images (FFIs) with 30 minute sampling. We reduced the data using the Quick Look pipeline of Huang et al. (2019). Two sequences of transit signals were detected: TOI-1130 b, with $P_b = 4.07$ days and a signal-to-noise ratio (S/N) of 24.2; and TOI-1130 c, with $P_c = 8.35$ days and S/N = 78.2. Both signals passed the standard vetting tests employed by the *TESS* Science Office, and the system was announced to the community as a *TESS* Object of Interest (TOI).

In an attempt to improve on the light curves produced by the automatic data reduction pipeline, we performed multi-aperture photometry of the publicly available FFIs that had been calibrated by the Science Processing Operation Center (Jenkins et al. 2016;

accessed via TESSCut[38]). Best results were obtained with a 3×3 pixel square aperture centered on the star. We omitted the data that were obtained at the beginning of the first spacecraft orbit (BJD 2458653.93 to 2458657.72) because the data quality was compromised by scattered moonlight.

The standard deviation of the time series of quaternions that the *TESS* spacecraft uses for attitude control has been shown to be correlated with systematic effects in *TESS* photometry. Therefore, we decorrelated the TOI-1130 light curve against the standard deviation of the Q1, Q2, and Q3 quaternion time series within each exposure, using a least-squares technique. During this procedure, we excluded the data obtained during transits. We also iterated several times, removing 3σ outliers from the fit until convergence (Vanderburg et al. 2019). This process did not remove a longer-term trend that was evident, but that is irrelevant for transit analysis. We modeled this slower variability by adding a fourth-order polynomial to the least-squares fit. Unlike Vanderburg et al. (2019), we did not perform high-pass-filtering of the quaternion time series before the decorrelation. Finally, we fitted a basis spline to the light curve to high-pass-filter any remaining long timescale variability (excluding transits and iteratively removing outliers; see Vanderburg & Johnson 2014).

2.2. Ground-based Time-series Photometry

We conducted ground-based seeing limited time-series photometric follow-up observations of TOI-1130 as part of the *TESS* Follow-up Observing Program (TFOP). To schedule these observations, we used the `TESS Transit Finder`, a customized version of the `Tapir` software package (Jensen 2013). Observations were made with the Las Cumbres Observatory Global Telescope (LCOGT; Brown et al. 2013[39]) network, the Perth Exoplanet Survey Telescope (PEST) in Australia, and the TRAPPIST-South telescope in Chile (Jehin et al. 2011; Gillon et al. 2013).

A full transit of the inner planet TOI-1130 b was observed in Pan-STARRS z_s-band on UT 2019 September 5 using a 1.0 m telescope at the LCOGT Siding Spring Observatory (SSO) node. The images from this observation and the other LCOGT observations were calibrated with the standard BANZAI pipeline and light curves were extracted using `AstroImageJ` (AIJ; Collins et al. 2017). An aperture radius of $2''$ was employed, which excluded most of the flux from a fainter star $4''$ away to the southeast ($\Delta T_{\mathrm{mag}} = 6.9$). The transit signal was clearly detected, with a duration and depth matching the *TESS* signal, thereby ruling out the faint star as the source of the signal. The bottom row of Figure 1 shows the light curve prepared with a $6''$ aperture, which gave a higher S/N than the $2''$ aperture. Based on the star catalog from *Gaia* Data Release 2 (DR2; Evans et al. 2018; Gaia Collaboration et al. 2018), there are two other stars within $20''$ of TOI-1130, but they are both too faint ($\Delta T_{\mathrm{mag}} = 8.6$ and 9.6) to be the source of the *TESS* signals.

We also observed one full transit of the hot Jupiter TOI-1130 c in the *Rc*-band with PEST on UT 2019 October 1. PEST is a $12''$ Meade LX200 SCT Schmidt–Cassegrain telescope equipped with a SBIG ST-8XME camera located in a suburb of Perth, Australia. A custom pipeline based on `C-Munipack`[40] was used to calibrate the images and extract

---

[38] https://mast.stsci.edu/tesscut/
[39] https://lco.global
[40] http://c-munipack.sourceforge.net
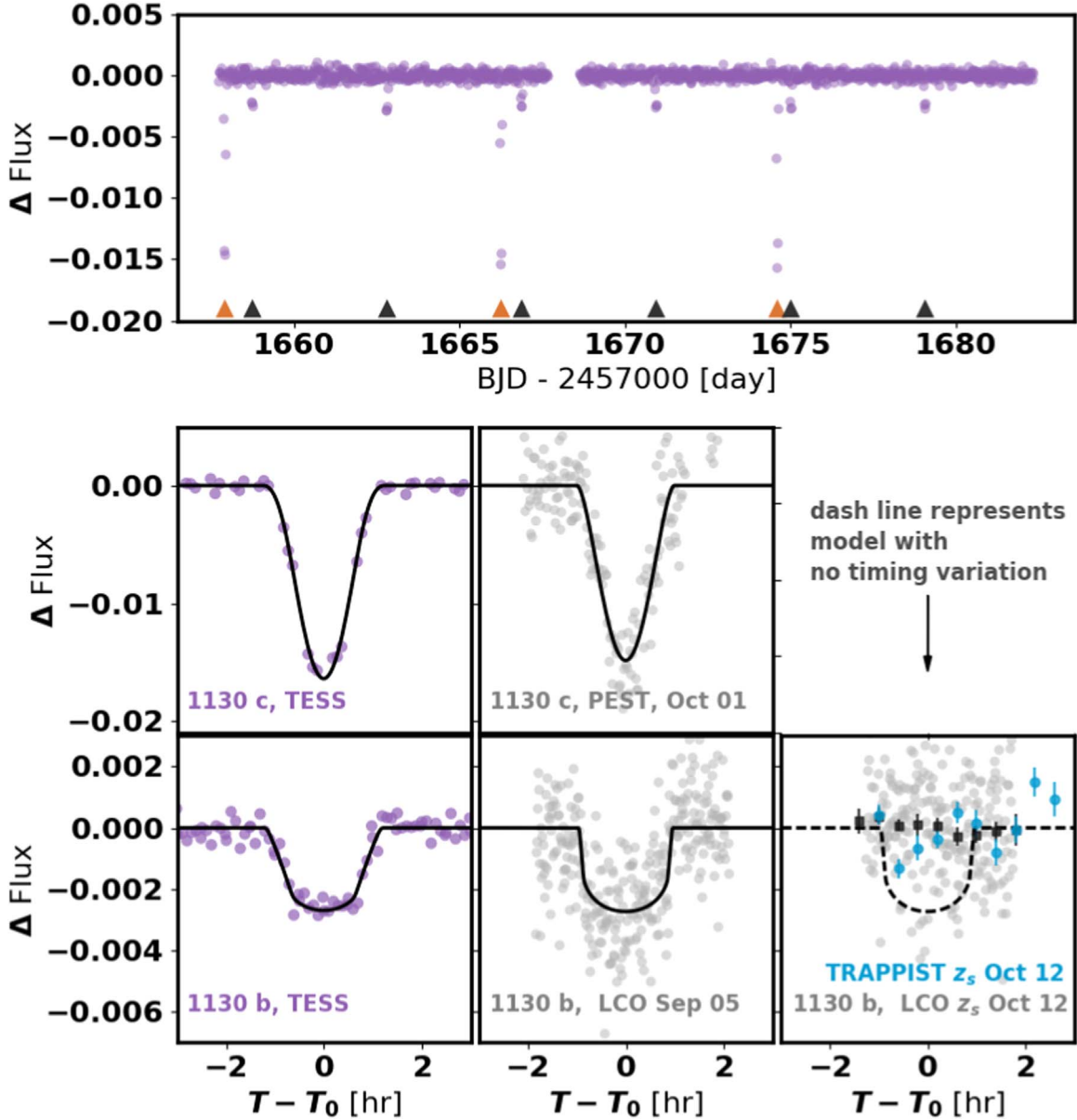
Figure 1. Light curve of TOI-1130. The top panel shows the detrended discovery light curve from *TESS*, in units of fractional deviations from the out-of-transit level. The triangles along the time axis mark the times of transits of the two planets. The middle panels show the phase-folded *TESS* light curve of the hot Jupiter as well as the follow-up light curve (gray points) from PEST obtained on UT 2019 October 1. The bottom panels show the phase-folded *TESS* light curve of the inner planet as well as follow-up light curves from the Las Cumbres Observatory. The middle bottom panels show z_s-band data from the Siding Spring Observatory node on 2019 September 5. The rightmost bottom panel shows the *non*-detection of the inner planet based on z_s-band observations from the Cerro Tololo node on 2019 October 12. The black squares represent time-averaged data. The blue points show time-averaged z_s-band data from TRAPPIST-South. The black lines in all of the panels represent the best-fitting model assuming strict periodicity of the transits.

the differential time-series photometry. The transiting event was detected using a $7.''4$ aperture centered on the target star.

We tried to observe another transit of TOI-1130 b in both the *B*- and z_s-bands on UT 2019 October 12 using a 1.0 m telescope at the Cerro Tololo Interamerican Observatory (CTIO) node of the LCOGT network. However, no transit signal was detected within the 3 hr span of the observations, which had been timed to coincide with the predicted time of transit. The prediction was based on the *TESS* data and the assumption of a strictly periodic orbit. We began observing half an hour prior to the predicted ingress time, and ended one hour after the predicted egress time. To make sure the transit could have been detected, we injected a transit signal with the appropriate characteristics into the LCOGT z_s-band light curve

at the predicted epoch, which made clear that the signal could have been detected at the 10σ level or higher. The data also show no evidence of an ingress or egress. Using the Bayesian information criterion comparing a transit model with the transit shape constrained by the *TESS* data and a flat, straight line model representing the scenario of no transit, we can confidently rule out that the center of transit happened inside the LCO observation baseline.

Moreover, the TRAPPIST-South telescope at La Silla was also used to observe the same transit in the Sloan z'-band. No transit was detected. Although the data are noisier than the LCO data, it is very likely that the transit would have been detected if it had occurred on schedule without any timing deviations. The non-detection is consistent with various
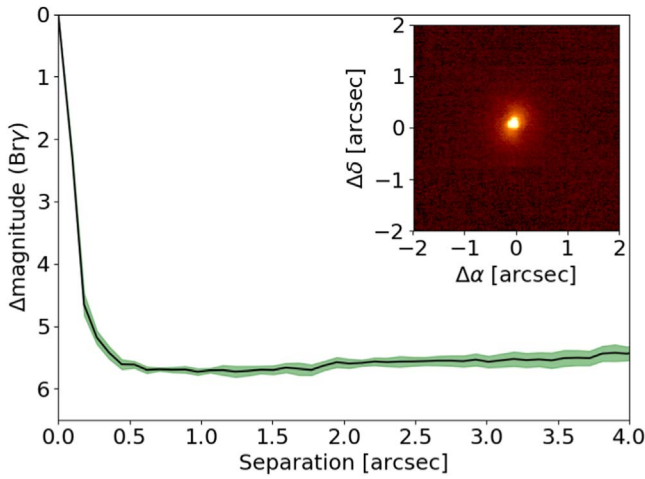
Figure 2. Brγ-band AO image from VLT NaCo (inset), and the resulting sensitivity to visual companions as a function of angular separation. No companions were detected within the field of view.

scenarios in which the Neptune experiences large transit-timing variations.

2.3. Adaptive-optics Images

Adaptive-optics (AO) images were collected on UT 2019 September 14 using Unit Telescope 4 of the Very Large Telescopes (VLTs) equipped with the Naos Conica (NaCo) instrument. We collected nine 20 s exposures with a Brγ filter. The telescope pointing was dithered by $2''$ in between exposures. Data reduction followed standard procedures using custom IDL codes: we removed bad pixels, flat-fielded the data, subtracted a sky background constructed from the dithered science frames, aligned the images, and co-added the data to obtain the final image. The sensitivity to faint companions was determined by injecting scaled point-spread functions at a variety of position angles and separations. The scaling was adjusted until the injected point sources could be detected with 5σ confidence. No companions were detected down to a contrast of 5.7 mag at $1''$. Figure 2 shows the sensitivity curve as a function of angular separation, along with a small image of the immediate environment of TOI-1130.

2.4. Radial Velocities (RVs)

We obtained a series of spectra of TOI-1130 using the CHIRON facility (Tokovinin et al. 2013) to monitor the star's RV variations and thereby measure or constrain the masses of the planets. CHIRON is a high-resolution spectrograph on the SMARTS 1.5 m telescope at CTIO. Light is delivered to the spectrograph via an image slicer and a fiber bundle, with a resolving power of 80,000 over the wavelength range from 4100 to 8700 Å. A total of 21 spectra were obtained between UT 2019 August 30 and UT 2019 October 17. There are no stars in the *Gaia* DR2 catalog that would have fallen within the CHIRON fiber ($2''.7$ in radius) that could contaminate the RVs.

The RVs were measured from the extracted spectra by modeling the least-squares deconvolution line profiles (Donati et al. 1997). Table 1 gives the results.

Table 1
RV for TOI-1130

Time	RV (km s^{-1})	Error (km s^{-1})
2458725.63420	−9.652	0.037
2458734.59335	−9.662	0.018
2458738.55132	−9.384	0.020
2458739.53575	−9.439	0.024
2458740.57420	−9.459	0.019
2458741.54135	−9.568	0.020
2458742.55255	−9.624	0.015
2458743.52740	−9.685	0.025
2458744.55082	−9.576	0.030
2458746.59182	−9.443	0.018
2458747.66486	−9.408	0.031
2458751.63354	−9.671	0.026
2458752.63038	−9.612	0.021
2458753.54111	−9.547	0.022
2458757.50133	−9.400	0.031
2458758.52657	−9.539	0.026
2458761.58060	−9.574	0.021
2458762.51420	−9.467	0.025
2458768.57449	−9.626	0.021
2458772.53023	−9.438	0.026
2458773.55102	−9.423	0.022

3. Analysis

3.1. Stellar Parameters

We determined the basic stellar parameters by fitting the observed spectral energy distribution (SED).[41] We compared the available broadband photometry with the M/K-dwarf spectral templates of Gaidos et al. (2014) and Kesseli et al. (2017). The details of this SED-fitting procedure were described by Mann et al. (2015) and are summarized here. For the photometry, we consulted the star catalogs from the Two-Micron All-Sky Survey (2MASS; Skrutskie et al. 2006), the *Wide-field Infrared Survey Explorer* (Wright et al. 2010), the *Gaia* DR2 (Evans et al. 2018; Gaia Collaboration et al. 2018), the AAVSO All-Sky Photometric Survey (APASS; Henden et al. 2012), and Tycho-2 (Høg et al. 2000). We compared the observed magnitudes to the synthetic magnitudes computed from each template spectrum, using Phoenix BT-SETTL models (Allard et al. 2011) to fill in the gaps in the spectra. We did not account for reddening or extinction, because the star is within the Local Bubble where these effects should be negligible. The resulting parameters are $T_{\rm eff} = 4250 \pm 67$ K, bolometric flux $= (1.42 \pm 0.05) \times 10^{-9}$ erg s^{-1} cm^{-2}, $L_\star = 0.150 \pm 0.006\,L_\odot$, and $R_\star = 0.714 \pm 0.029\,R_\odot$. The best-fitting template and model combination gave a minimum reduced chi-squared of 0.8, indicating a good fit. These results are consistent with the standard stellar SED-fitting method using the NextGen stellar atmosphere models (Stassun et al. 2018, 2019), which gave $T_{\rm eff} = 4300 \pm 100$ K, and $R_\star = 0.692 \pm 0.032 R_\odot$.

The SED fit strongly favors a metal-rich composition. All of the templates with a solar or sub-solar metallicity gave $\chi^2_\nu > 3$. The *Gaia* data also reveals that the M_G absolute magnitude of TOI-1130 places it within the brightest 10% of stars with the same $BP - RP$ color. Since late-K dwarfs do not evolve

---

[41] We also derived the best-fitting stellar parameters from the average CHIRON spectra, yielding $T_{\rm eff} = 4545 \pm 14$ K, $\log g_\star = 4.60 \pm 0.038$ dex, [m/H] $= -0.105 \pm 0.063$ dex, and $v \sin I_\star = 4$ km s^{-1}. However, because the library is not well calibrated for low-mass stars, we did not rely on these CHIRON-based parameters in the subsequent analysis.

significantly over the lifetime of the universe, this high position in the color–magnitude diagram is best explained by a high metallicity. (The possibility of an unresolved stellar companion is ruled out by the AO imaging presented above.) Based on the expected distribution of metallicities in the Solar neighborhood, we infer that TOI-1130 has a metal content [M/H] > 0.2.

We estimated $M_\star$ using the empirical relation between M_{K_S} and mass from (Mann et al. 2019).[42] This relation was calibrated using dynamical masses of K- and M-dwarf binaries. The result is $M_\star = 0.671 \pm 0.018\,M_\odot$.

3.2. Global Modeling

We performed a joint analysis of the *TESS* transit light curve, the 21 RV from CHIRON, and the ground-based follow-up light curves excluding the October 12 observations. We restricted the orbital eccentricity of TOI-1130 c to be smaller than 0.2. Numerical integrations showed that the system would not be stable for more than 10^5 years if the eccentricity were any larger. We also allowed for a radial-velocity "jitter" term, which was added in quadrature to the nominal uncertainties to account for unmodeled systematic and astrophysical effects. We did not include the effects of TOI-1130 b in the radial-velocity model, because the expected radial-velocity amplitude is beneath the 10 m s^{-1} level.

We assumed that the stellar limb-darkening follows a quadratic law and used the formulas of Mandel & Agol (2002) as implemented by Kreidberg (2015) while modeling the transit light curves. We set priors on the limb-darkening coefficients using the LDTk model implemented by Parviainen & Aigrain (2015) based on a library of PHOENIX-generated specific intensity spectra by Husser et al. (2013). The resulting limb-darkening coefficients are consistent with the values tabulated by Claret (2017) and Claret et al. (2012). The duration of the transits from both planets are relatively short (∼2 hours), to account for the 30 minute averaging time of the *TESS* data, the photometric model was computed with 1 minute sampling and then averaged to 30 minutes (Kipping 2010).

The mass and radius of the star were also adjustable parameters, with priors based on the results presented in Section 3.1. Another constraint on these parameters came from the implicit value of the stellar mean density $\rho_\star$ that arises from the combination of P, $a/R_\star$, and i (Seager & Mallén-Ornelas 2003; Winn 2010). The likelihood function enforced agreement with the measurements of $\rho_\star$ from the posterior determined by the SED modeling.

To determine the credible intervals for all the parameters, we used the "emcee" Markov Chain Monte Carlo method of Foreman-Mackey et al. (2013). The results are given in Table 2, and the best-fitting model is plotted in Figures 1 and 3. For a "second opinion" on the model parameters, we used the EXOFASTv2 code (Eastman et al. 2013, 2019) to fit the same data. The results all agreed to within 0.5σ or better.

The model assumed the transits to be strictly periodic, despite the evidence for transit-timing variations (TTVs) presented earlier. We did not account for the October 12 observation in our global modeling. For this reason, we caution that the uncertainties in the orbital periods are likely larger than are reported in Table 2. This is especially true for the lower-mass planet TOI-1130 b. Further photometric observations are needed to get a better understanding of the periods and the timing variations.

Table 2
System Parameters for TOI-1130

Parameters	Values	Comments
Catalog Information		
R.A. (h:m:s)	19:05:30.24	*Gaia* DR2
Decl. (d:m:s)	−41:26:15.49	*Gaia* DR2
Epoch	2015.5	*Gaia* DR2
Parallax (mas)	17.13 ± 0.049	*Gaia* DR2
$\mu_{R.A.}$ (mas yr^{-1})	12.54 ± 0.088	*Gaia* DR2
$\mu_{decl.}$ (mas yr^{-1})	−27.18 ± 0.071	*Gaia* DR2
Gaia DR2 ID	6715688452614516736	
Tycho ID	TYC 7925-02200-1	
TIC ID	254113311	
TOI ID	1130	
Photometric Properties		
B (mag)	12.632	APASS
V (mag)	11.368	APASS
TESS (mag)	10.143	TIC V8
Gaia (mag)	10.902	*Gaia* DR2
Gaia$_r$ (mag)	10.092	*Gaia* DR2
Gaia$_b$ (mag)	11.653	*Gaia* DR2
J (mag)	9.055 ± 0.023	2MASS
H (mag)	8.493 ± 0.059	2MASS
K$_s$ (mag)	8.351 ± 0.033	2MASS
Stellar Properties		
T_{eff} (K)	4250 ± 67	SED
$\log g$ (cgs)	$4.60^{+0.02}_{-0.018}$	this work
[Fe/H] (dex)	>0.2	SED
$v \sin i$ (km s^{-1})	4.0 ± 0.5	SPC
$M_\star$ ($M_\odot$)	$0.684^{+0.016}_{-0.017}$	this work
$R_\star$ ($R_\odot$)	$0.687^{+0.015}_{-0.015}$	this work
$L_\star$ ($L_\odot$)	$0.140^{+0.011}_{-0.010}$	this work
Age (Gyr)	$8.2^{+3.8}_{-4.9}$	this work
Distance (pc)	58.26 ± 0.17	*Gaia* DR2
$\rho_\star$ (g cm^{-3})	$2.97^{+0.20}_{-0.17}$	this work
$u_{1,tess}$	0.49 ± 0.05	this work
$u_{2,tess}$	0.06 ± 0.05	this work
u_{1,z_S}	0.46 ± 0.05	this work
u_{2,z_S}	0.13 ± 0.05	this work
u_{1,R_C}	0.72 ± 0.05	this work
u_{2,R_C}	0.06 ± 0.03	this work
Additional RV Parameters		
γ(km s^{-1})	$-9.5241^{+0.0041}_{-0.0040}$	
jitter (km s^{-1})	$0.0112^{+0.0066}_{-0.0069}$	
Planet Parameters	b	c
P (days)	$4.066499^{+0.000046}_{-0.000045}$	$8.350381^{+0.000032}_{-0.000033}$
T_c (BJD)	$2458658.74627^{+0.00072}_{-0.00068}$	$2458657.90461^{+0.00021}_{-0.00022}$
K (km s^{-1})		$0.1259^{+0.0052}_{-0.0055}$
$\sqrt{e}\cos\omega$	$0.26^{+0.13}_{-0.17}$	$-0.093^{+0.079}_{-0.072}$
$\sqrt{e}\sin\omega$	$0.33^{+0.19}_{-0.33}$	$0.17^{+0.11}_{-0.16}$
e	$0.22^{+0.11}_{-0.11}$	$0.047^{+0.040}_{-0.027}$
ω	...	-28^{+24}_{-55}
T_{14} (hr)	$2.30^{+0.18}_{-0.14}$	$2.02^{+0.044}_{-0.044}$
$a/R_\star$	$13.75^{+0.31}_{-0.27}$	$22.21^{+0.50}_{-0.43}$
$R_p/R_\star$	$0.04860^{+0.00111}_{-0.00090}$	$0.218^{+0.037}_{-0.029}$
$b \equiv a\cos i/R_\star$	$0.48^{+0.11}_{-0.21}$	$0.995^{+0.046}_{-0.043}$
i_c (deg)	$87.98^{+0.86}_{-0.46}$	$87.43^{+0.16}_{-0.16}$
M_p	...	$0.974^{+0.043}_{-0.044}\,M_J$
R_p	$3.65^{+0.10}_{-0.10}\,R_\oplus$	$1.50^{+0.27}_{-0.22}\,R_J$
ρ_p (g cm^{-3})	...	$0.38^{+0.24}_{-0.15}$
a (au)	$0.04394^{+0.00035}_{-0.00038}$	$0.07098^{+0.00056}_{-0.00060}$
T_{eq}[a] (K)	810^{+15}_{-15}	637^{+12}_{-12}

Note.
[a] The equilibrium temperatures are derived assuming zero albedo for both planets.
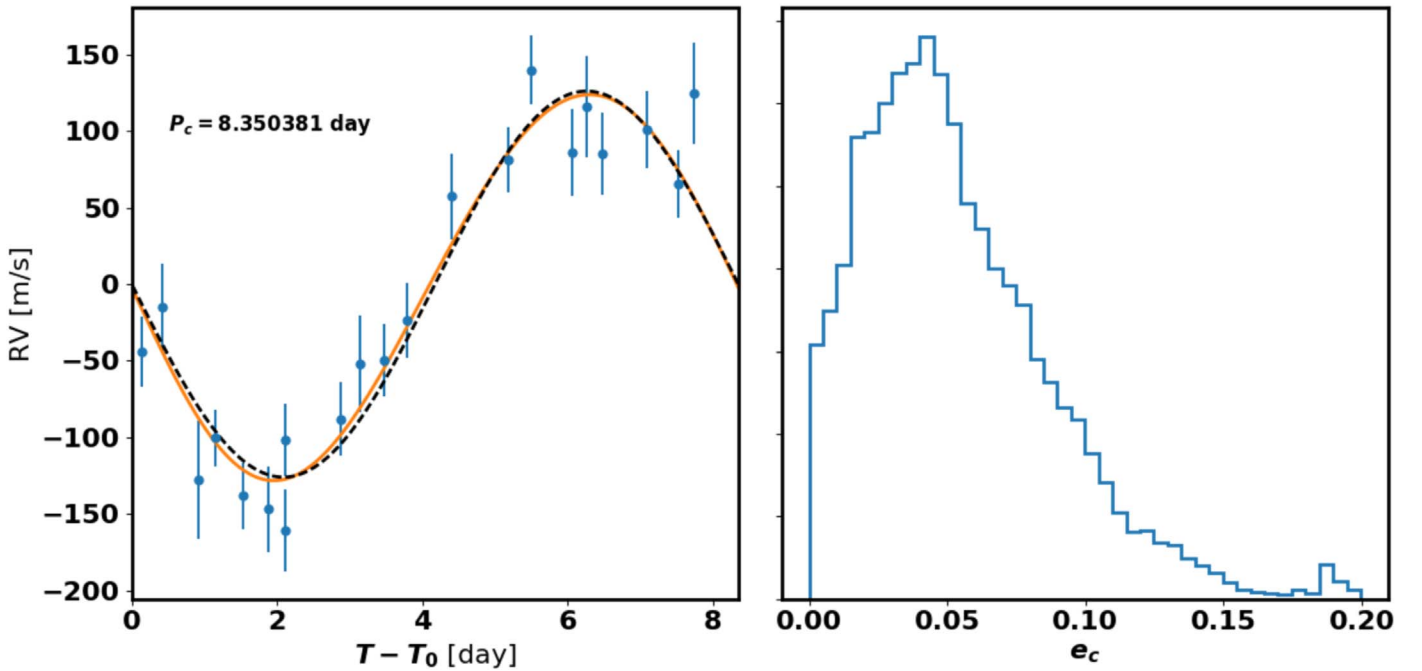
Figure 3. Left panel: relative radial-velocity orbit of TOI-1130 c based on CHIRON data. The plotted error bars include the "jitter" term described in Section 3. The orange line is the best-fitting model. The black dashed line represents a circular orbit with the same semi-amplitude. Right panel: posterior probability distribution for the orbital eccentricity.

3.3. Confirmation of TOI-1130 c

The mass of TOI-1130 c was found to be $0.974^{+0.043}_{-0.044}$ M_J. The radius of the planet is not well constrained because the transit is grazing. However, based on the mass of the planet, we put a prior constraint on the radius of the planet to be less than 2 R_J, and are able to determine the radius to be $1.50^{+0.27}_{-0.22}$ R_J. The orbit of TOI-1130 c appears to be slightly eccentric, $e = 0.047^{+0.040}_{-0.027}$. Modeling the CHIRON RVs alone would give a more eccentric solution for TOI-1130 c, $e = 0.074 \pm 0.023$. Future monitoring will refine the eccentricity constraint.

3.4. Validation of TOI-1130 b

The CHIRON data are not precise enough to reveal the RV signal of TOI-1130 b. An upper limit on the mass of TOI-1130 b was obtained by fitting a two-planet model to the RV data, using the posterior of the global modeling to constraint the period and epoch of both planets. We allow the semi-amplitude to be negative in the fit. The resulting 3σ upper limit is 40 $M_\oplus$. Even though the RV signal was not detected, there is a 2σ hint that the orbit of TOI-1130 b is eccentric, based on the combination of the transit duration, transit impact parameter, and the observational constraints on the mean stellar density.

Without a RV detection, one must proceed with care to make sure that the *TESS* transit signals really arise from a planet around the target star, and not an unresolved background eclipsing binary or other type of "false positive." The transit signals seen by TOI-1130 b in *TESS* and LCOGT have a flat bottom, in contrast to the V-shaped appearance of most eclipsing binaries.

A more quantitative argument can be made based on the ratio between the duration of ingress or egress and the duration of the flat-bottomed portion of the transit (Seager & Mallén-Ornelas 2003). This ratio is observed to be $T_{12}/T_{13} = 0.064 \pm 0.02$. For an isolated star with an eclipsing companion, this ratio is equal to the maximum possible radius ratio between the eclipsing object and the star. The corresponding maximum flux deficit is the

square of the radius ratio, giving a 2σ upper limit on the flux deficit of 0.007. To produce such a signal, a blended stellar companion would need to be within 1.23 mag of TOI-1130. The AO image presented in Section 2 rules out such a companion beyond $1''$ (a projected separation of $\sim$58 au). Based on the lack of any long-term trend in the CHIRON RV data, we are also able to place a 3σ upper limit of 0.318 $M_\odot$ (Δ mag $\lesssim 2.6$) on any bound companion within 4 au.

We used vespa (Morton 2015) to evaluate the probability of any remaining false-positive scenarios involving eclipsing binaries. Using the *TESS* light curve of TOI-1130 b and the constraints from spectroscopy and imaging, vespa returns a false-positive probability of FPP $< 10^{-6}$. Thus, we consider TOI-1130 b to be a validated planet. Section 4.1 presents further evidence that this planet orbits the same star as TOI-1130 c, based on the tentative detection of TTVs.

4. Discussion

4.1. Dynamical Constraints

Dynamical simulations were conducted, with the hope of improving our knowledge of the system parameters by requiring that they be consistent with long-term stability. We also wanted to see if TTVs due to planet–planet interactions could plausibly be large enough to explain the "missing transit" on 2019 October 12.

4.1.1. System Stability

We performed three suites of simulations using Mercury6 (Chambers 1999). The first two suites were composed of 100 simulations each. The initial conditions for each simulation were selected from a randomly chosen link in the posterior produced by the analysis described in Section 3. However, because the mass, eccentricity, and argument of pericenter ω of the inner planet are poorly constrained, the initial values of

those parameters were handled differently. The mass of the planet was set equal to that of Neptune. In the first suite of simulations, we set the initial eccentricity equal to zero. In the second suite, we drew e and ω from uniform distributions with ranges of $0°.0$–$0°.3$ and $0°$–$360°$, respectively.

We used a time-step of 20 minutes to integrate the equations of motion for 10^5 yr, used the hybrid symplectic and Bulirsch–Stoer integrator, and enforced energy conservation to within one part in 10^8 or better.

In both suites of simulations, the vast majority of initial conditions led to stable configurations; i.e., they did not experience orbit crossings, collisions, or ejections during the simulation time. In the first suite, all 100 trials were consistent with stability. In the second suite, 96 were stable. The four unstable trials involved some of the highest initial eccentricities for both planets. These experiments suggest that if TOI-1130 b has a low eccentricity, essentially the full range of system parameters consistent with the data are also consistent with dynamical stability. A moderate eccentricity for the inner planet is also generally consistent with long-term stability.

In the stable configurations, the planetary eccentricities oscillate. For TOI-1130 b, the forced eccentricity is the most important component. The largest value obtained in the dynamically stable trials of either suite was about 0.30. The typical value of upper envelope of the eccentricity oscillations was closer to 0.17. The relative contributions of the free and forced eccentricities can be determined better through future observations of the phase of the TTVs.

The third suite of simulations, composed of 500 integrations, was intended to study the planetary eccentricities in more detail. We tested a large range of possible eccentricities for both planets (while randomizing ω). The inner planet was assumed to have the same mass as Neptune. The outer planet's mass was drawn from the posterior, along with all of the other system parameters. Dynamical stability was seen in all the trials for which the eccentricities obeyed the relation $e_b + 2e_c < 0.4$. When this inequality was violated, instability was more likely. If e_b rose above 0.4 or 0.5, the system was nearly always unstable.

4.1.2. TTVs

As described in Section 2, the two attempts to observe the transit of 2019 October 12 resulted in flat light curves, ruling out the occurrence of a transit at the predicted time. Could this plausibly be due to a large TTV caused by planet–planet interactions?

The ratio between the orbital periods of the two planets is within 2.5% of 2:1, implying that the system is close to resonance. This condition usually results in large TTVs. Based on the current best estimates of the orbital periods, the super period of the expected TTVs, computed using the analytic theory of Lithwick et al. (2012), is between about 156 and 156.5 days. Inflating the error on each orbital period to 1.5 minutes, however, increases the uncertainty on the super period by of a factor of 16 to about 8 days. Although the super period is fairly well constrained, the expected amplitude of the timing variations is poorly constrained. The unknown mass of the inner planet leads to estimates for the TTV amplitudes ranging from seconds to hours.

Figure 4 shows the dependence of the TTV amplitude on the mass and eccentricity of the inner planet. The TTV amplitude was computed using TTVFast (Deck et al. 2014). In these Monte Carlo trials, the stellar parameters and those of the outer
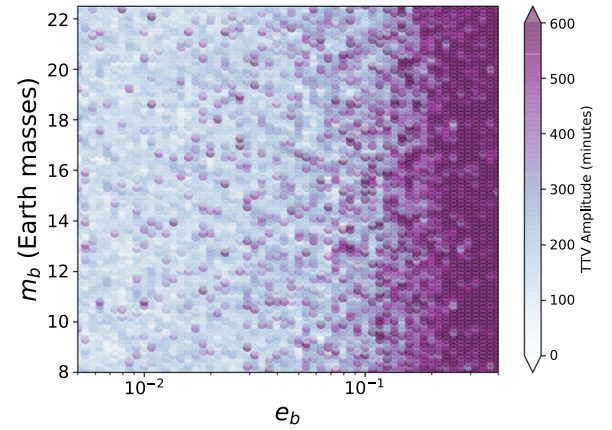
Figure 4. Monte Carlo exploration of the theoretical TTV amplitude as a function of the mass and eccentricity of TOI-1130 b. Each point corresponds to one link drawn from the posterior. The color encodes the TTV amplitude. For eccentricities exceeding about 0.01, the typical TTV amplitude is on the order of hours, which is large enough to explain the non-detection of the October 12 transit.

planet's orbital elements were drawn from the posterior, while the inner planet's mass and eccentricity were sampled uniformly between the limits shown on the plot. The argument of pericenter was drawn randomly from a uniform distribution. To explain the October transit non-detection, we require a TTV amplitude of at least two hours. The majority of parameter space is expected to give TTV amplitudes at this level or above. Thus, TTVs are indeed a plausible explanation.

4.2. TOI-1130's Place in the Hot Jupiter Paradigm

Figure 5 illustrates the period distribution of transiting giant planets with transiting inner companions. The only three transiting hot Jupiters ($P < 10$ days) known to have inner transiting companions are WASP-47 b, Kepler-730 b, and TOI-1130 c. Their orbital periods are 4.2 days, 6.5 days, and 8.4 days, respectively. Other giant planets with somewhat longer orbital periods—"warm Jupiters"—are more frequently found with inner companions (Huang et al. 2016).

The apparently continuous period distribution of the giant planets in Figure 5 suggests that the hot Jupiters with inner companions are not so different from the warm Jupiters with inner companions. Perhaps both types of systems are produced by the same process, and the hot Jupiters with companions represent the tail of a statistical distribution of outcomes. In that case, the more commonly encountered "lonely" hot Jupiters (without close companions) might have formed from a different mechanism.

Comparison of Figure 5 with similar figures that have been made for *Kepler* systems in general (see, e.g., Fabrycky et al. 2014) suggest that the systems with giant planets and small inner companions resemble the closely packed and coplanar *Kepler* multi-planet systems of super-Earths. The giant-planet systems simply have more extreme size and mass ratios between the planets. Specifically, in *Kepler* multi-planet systems in general (which mostly contain sub-Neptune-sized planets, the typical Hill spacing is 21.7 ± 9.5 (e.g., Fang & Margot 2013; Weiss et al. 2018)). The typical mutual Hill radii of the planets in Figure 5 is 16.8 ± 9.6. We speculate that all these close-orbiting multi-planet systems originated from essentially the same process, but in rare cases, one of the super-Earths managed to exceed the threshold mass for runaway gas accretion (Lee et al. 2014; Batygin et al. 2016). Such rare cases may lead to the formation of the systems shown in Figure 5.
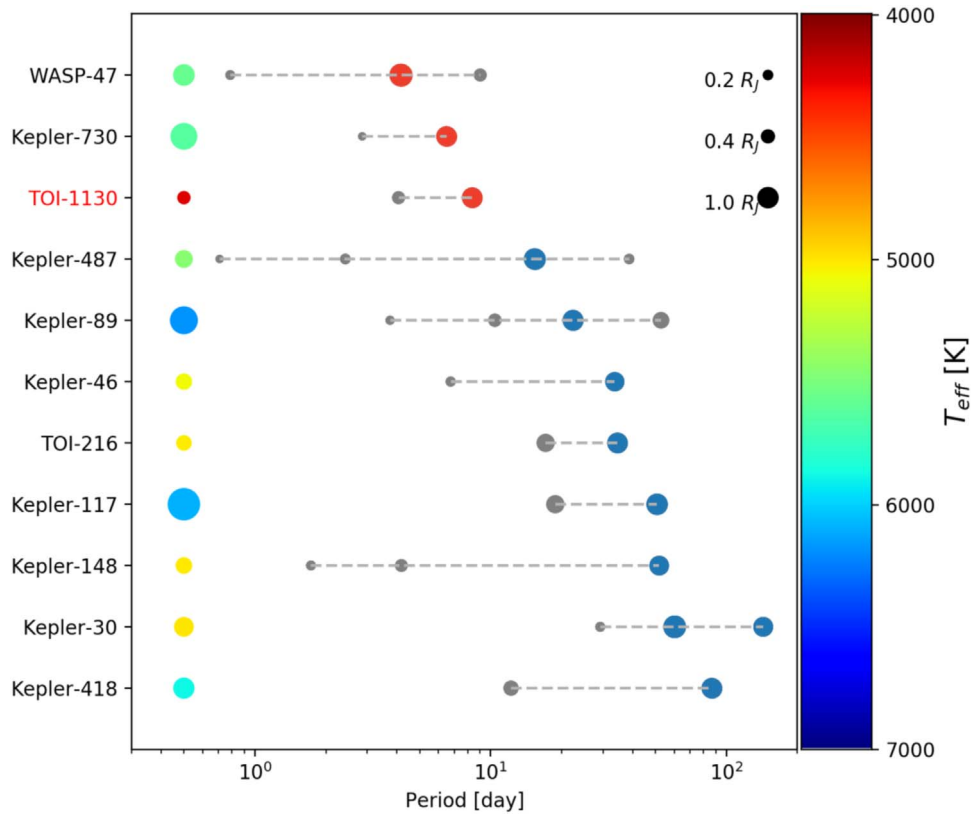
Figure 5. All confirmed planetary systems consisting of a transiting giant planet with period shorter than 100 days and inner transiting companions. Each horizontal line represents a planetary system. The giant planets with period smaller (larger) than 10 days are represented by red (blue) circles, and the small planets are represented by gray circles. The first circle in each line represent the host star, color coded with their effective temperature. The sizes of the circles are proportional to the radii of planets.

One reason why it would be interesting to further enlarge the sample of giant planets with small inner companions is to study the distribution of period ratios, and the proximity to resonances. In all three cases of hot Jupiters with inner companions, none of the known planets are in resonance. Only a small fraction of the *Kepler* multi-planet systems are in resonance (Lissauer et al. 2011), while systems of multiple wide-orbiting giant planets are frequently in resonance (Winn & Fabrycky 2015). It would therefore be interesting to know how frequently systems with giant planets and small inner companions are in resonance. If these systems and the super-Earth systems both assembled via the same mechanism, then one might expect the period ratio distributions (including the occurrence of resonances) to be similar.

TOI-1130 has a brighter host star than WASP-47 or Kepler-730, which will facilitate follow-up opportunities to investigate the mystery the formation of these types of systems. For example, the expected Rossiter–McLaughlin amplitudes of the two planets (6 and 7 m s^{-1})[43] are detectable with current facilities for a star as bright as TOI-1130. These measurements can reveal the stellar obliquity and mutual inclination between the orbits, both of which are relevant to the formation mechanism. Additionally, TOI-1130 is a K7 star, which is the smallest star known to host similar type of system architecture to date. It is relatively bright at near-infrared wavelengths ($K_s = 8.351$), making the planet a good target for

transit spectroscopy to study planetary atmospheres. Specifically, the atmospheric signal of TOI-1130 c is probably detectable with the *Hubble Space Telescope.* Comparisons between its atmosphere and that of the other hot and warm Jupiters may help us understand its origin.

The discovery of TOI-1130 illustrates *TESS*'s power to find systems with rare architectures. With a large amount of *TESS* data still unexplored, we can expect more systems such as TOI-1130, along with better knowledge of the frequencies of different types of hot Jupiter systems.

---

[43] Even though the transit of TOI 1130 c is significantly deeper than that of TOI 1130 b, we expect they will have similar Rossiter–McLaughlin amplitudes because of TOI 1130 c's high impact parameter.

ORCID iDs

Chelsea X. Huang ⓘ https://orcid.org/0000-0003-0918-7484
Samuel N. Quinn ⓘ https://orcid.org/0000-0002-8964-8377
Andrew Vanderburg ⓘ https://orcid.org/0000-0001-7246-5438
Juliette Becker ⓘ https://orcid.org/0000-0002-7733-4522
Joseph E. Rodriguez ⓘ https://orcid.org/0000-0001-8812-0565
Francisco J. Pozuelos ⓘ https://orcid.org/0000-0003-1572-7707
Davide Gandolfi ⓘ https://orcid.org/0000-0001-8627-9628
George Zhou ⓘ https://orcid.org/0000-0002-4891-3517
Andrew W. Mann ⓘ https://orcid.org/0000-0003-3654-1602
Karen A. Collins ⓘ https://orcid.org/0000-0001-6588-9574
Kevin I. Collins ⓘ https://orcid.org/0000-0003-2781-3207
Malcolm Fridlund ⓘ https://orcid.org/0000-0003-2180-9936
Michaël Gillon ⓘ https://orcid.org/0000-0003-1462-7739
Maximilian N. Günther ⓘ https://orcid.org/0000-0002-3164-9086
Eric L. N. Jensen ⓘ https://orcid.org/0000-0002-4625-7333
Stephen R. Kane ⓘ https://orcid.org/0000-0002-7084-0529
Rachel A. Matson ⓘ https://orcid.org/0000-0001-7233-7508
Keivan G. Stassun ⓘ https://orcid.org/0000-0002-3481-9052
Avi Shporer ⓘ https://orcid.org/0000-0002-1836-3120
Lizhou Sha ⓘ https://orcid.org/0000-0001-5401-8079
Thiam-Guan Tan ⓘ https://orcid.org/0000-0001-5603-6895
Savita Mathur ⓘ https://orcid.org/0000-0002-0129-0316
Roland K. Vanderspek ⓘ https://orcid.org/0000-0001-6763-6562
David W. Latham ⓘ https://orcid.org/0000-0001-9911-7388
Joshua N. Winn ⓘ https://orcid.org/0000-0002-4265-047X
S. Seager ⓘ https://orcid.org/0000-0002-6892-6948
Jon M. Jenkins ⓘ https://orcid.org/0000-0002-4715-9460
Christopher J. Burke ⓘ https://orcid.org/0000-0002-7754-9486
Mark E. Rose ⓘ https://orcid.org/0000-0003-4724-745X
Eric B. Ting ⓘ https://orcid.org/0000-0002-8219-9505
Guillermo Torres ⓘ https://orcid.org/0000-0002-5286-0251
Ian Wong ⓘ https://orcid.org/0000-0001-9665-8429

References

Allard, F., Homeier, D., & Freytag, B. 2011, in ASP Conf. Ser. 448, 16th Cambridge Workshop on Cool Stars, Stellar Systems, and the Sun, ed. C. Johns-Krull, M. K. Browning, & A. A. West (San Francisco, CA: ASP), 91
Batygin, K., Bodenheimer, P. H., & Laughlin, G. P. 2016, ApJ, 829, 114
Becker, J. C., Vanderburg, A., Adams, F. C., Rappaport, S. A., & Schwengeler, H. M. 2015, ApJL, 812, L18
Brown, T. M., Baliber, N., Bianco, F. B., et al. 2013, PASP, 125, 1031
Cañas, C. I., Wang, S., Mahadevan, S., et al. 2019, ApJL, 870, L17
Chambers, J. E. 1999, MNRAS, 304, 793
Claret, A. 2017, A&A, 600, A30
Claret, A., Hauschildt, P. H., & Witte, S. 2012, A&A, 546, A14
Collins, K. A., Kielkopf, J. F., Stassun, K. G., & Hessman, F. V. 2017, AJ, 153, 77
Dawson, R. I., & Johnson, J. A. 2018, ARA&A, 56, 175
Deck, K. M., Agol, E., Holman, M. J., & Nesvorný, D. 2014, ApJ, 787, 132
Donati, J.-F., Semel, M., Carter, B. D., Rees, D. E., & Collier Cameron, A. 1997, MNRAS, 291, 658
Eastman, J., Gaudi, B. S., & Agol, E. 2013, PASP, 125, 83
Eastman, J. D., Rodriguez, J. E., Agol, E., et al. 2019, arXiv:1907.09480
Evans, D. W., Riello, M., De Angeli, F., et al. 2018, A&A, 616, A4
Fabrycky, D. C., Lissauer, J. J., Ragozzine, D., et al. 2014, ApJ, 790, 146
Fang, J., & Margot, J.-L. 2013, ApJ, 767, 115
Foreman-Mackey, D., Hogg, D. W., Lang, D., & Goodman, J. 2013, PASP, 125, 306
Gaia Collaboration, Brown, A. G. A., Vallenari, A., et al. 2018, A&A, 616, A1
Gaidos, E., Mann, A. W., Lépine, S., et al. 2014, MNRAS, 443, 2561
Gillon, M., Jehin, E., Fumel, A., Magain, P., & Queloz, D. 2013, EPJWC, 47, 03001
Henden, A. A., Levine, S. E., Terrell, D., Smith, T. C., & Welch, D. 2012, JAVSO, 40, 430
Høg, E., Fabricius, C., Makarov, V. V., et al. 2000, A&A, 355, L27
Huang, C., Wu, Y., & Triaud, A. H. M. J. 2016, ApJ, 825, 98
Huang, C. X., Burt, J., Vanderburg, A., et al. 2018, ApJL, 868, L39
Huang, X., Burt, J., Vanderburg, A., et al. 2019, AAS Meeting, 233, 209.08
Husser, T.-O., Wende-von Berg, S., Dreizler, S., et al. 2013, A&A, 553, A6
Jehin, E., Gillon, M., Queloz, D., et al. 2011, Msngr, 145, 2
Jenkins, J. M., Twicken, J. D., McCauliff, S., et al. 2016, Proc. SPIE, 9913, 99133E
Jensen, E. 2013, Tapir: A Web Interface for Transit/Eclipse Observability, Astrophysics Source Code Library, ascl:1306.007
Kesseli, A. Y., West, A. A., Veyette, M., et al. 2017, ApJS, 230, 16
Kipping, D. M. 2010, MNRAS, 408, 1758
Kreidberg, L. 2015, PASP, 127, 1161
Lee, E. J., Chiang, E., & Ormel, C. W. 2014, ApJ, 797, 95
Lissauer, J. J., Ragozzine, D., Fabrycky, D. C., et al. 2011, ApJS, 197, 8
Lithwick, Y., Xie, J., & Wu, Y. 2012, ApJ, 761, 122
Mandel, K., & Agol, E. 2002, ApJL, 580, L171
Mann, A. W., Dupuy, T., Kraus, A. L., et al. 2019, ApJ, 871, 63
Mann, A. W., Feiden, G. A., Gaidos, E., Boyajian, T., & von Braun, K. 2015, ApJ, 804, 64
Mayor, M., & Queloz, D. 1995, Natur, 378, 355
Morton, T. D. 2015, VESPA: False Positive Probabilities Calculator, Version 0.6, Astrophysics Source Code Library, ascl:1503.011
Parviainen, H., & Aigrain, S. 2015, MNRAS, 453, 3821
Rein, H., & Liu, S.-F. 2012, A&A, 537, A128
Ricker, G. R., Winn, J. N., Vanderspek, R., et al. 2015, JATIS, 1, 014003
Rossum, G. 1995, Python Reference Manual, CWI Tech. Rep.
Schlaufman, K. C., & Winn, J. N. 2016, ApJ, 825, 62
Seager, S., & Mallén-Ornelas, G. 2003, ApJ, 585, 1038
Skrutskie, M. F., Cutri, R. M., Stiening, R., et al. 2006, AJ, 131, 1163
Stassun, K. G., Corsaro, E., Pepper, J. A., & Gaudi, B. S. 2018, AJ, 155, 22
Stassun, K. G., Oelkers, R. J., Paegert, M., et al. 2019, AJ, 158, 138
Steffen, J. H., Ragozzine, D., Fabrycky, D. C., et al. 2012, PNAS, 109, 7982
Sullivan, P. W., Winn, J. N., Berta-Thompson, Z. K., et al. 2015, ApJ, 809, 77
Tokovinin, A., Fischer, D. A., Bonati, M., et al. 2013, PASP, 125, 1336
van der Walt, S., Colbert, S. C., & Varoquaux, G. 2011, CSE, 13, 22
Vanderburg, A., Huang, C. X., Rodriguez, J. E., et al. 2019, ApJL, 881, L19
Vanderburg, A., & Johnson, J. A. 2014, PASP, 126, 948
Weiss, L. M., Marcy, G. W., Petigura, E. A., et al. 2018, AJ, 155, 48
Winn, J. N. 2010, in Exoplanets, ed. S. Seager (Tucson, AZ: Univ. Arizona Press), 55
Winn, J. N., & Fabrycky, D. C. 2015, ARA&A, 53, 409
Wright, E. L., Eisenhardt, P. R. M., Mainzer, A. K., et al. 2010, AJ, 140, 1868
Zhu, W., Dai, F., & Masuda, K. 2018, RNAAS, 2, 160